Nano Research

Open Access

Research Article

The Co^{2+}-induced synergistic effect in nickel 5-methylsalicylate MOFs electrocatalysts for enhanced glucose electrooxidation

Qing Li[1] ✉, Yuan Li[4,7], Sicong Zhang[2], Xinyu Qin[2], Dianhui Wang[2,8], Boyan Tai[1,3], Mohsen Shakouri[5], Bin He[6], and Huan Pang[2] ✉

[1] *Guangling College, Yangzhou University, Yangzhou 225009, China*
[2] *School of Chemistry and Materials, Yangzhou University, Yangzhou 225009, China*
[3] *Interdisciplinary Research Center for Advanced Energy, Yangzhou University, Yangzhou 225127, China*
[4] *Key Laboratory for Green Processing of Chemical Engineering of Xinjiang Bingtuan, School of Chemistry and Chemical Engineering, Shihezi University, Shihezi 832003, China*
[5] *Canadian Light Source Inc., University of Saskatchewan, Saskatoon S7N 2V3, Canada*
[6] *Zhejiang Key Laboratory for Industrial Solid Waste Thermal Hydrolysis Technology and Intelligent Equipment, Huzhou Key Laboratory of Environmental Functional Materials and Pollution Control, Department of Materials Engineering, Huzhou University, Huzhou 313000, China*
[7] *School of Environmental Science, Nanjing Xiaozhuang University, Nanjing 211171, China*
[8] *School of Chemistry and Chemical Engineering, Chongqing University of Science and Technology, Chongqing 401331, China*

Cite this article: *Nano Research*, **2026**, *19*, 94908377. https://doi.org/10.26599/NR.2026.94908377

ABSTRACT: Strategically tailoring the electronic configuration of electrocatalysts through the incorporation of additional metal ions serves as a highly effective approach for boosting electrochemical glucose oxidation performance. In this work, a series of Co-doped nickel 5-methylsalicate (MeSA) metal organic framework (MOF) composites (NiCo-MeSA) were developed via a one-step solvothermal method. The NiCo-MeSA complex exhibits a porous MOF structure, promoting the electrolyte diffusion and access to active sites. Moreover, the introduction of Co^{2+} effectively regulates the electronic structure of Ni-MeSA catalysts, thereby improving both the selectivity toward glucose and stability of electrochemical glucose oxidation reaction (GOR). The optimized NiCo-MeSA nanocomposites demonstrate high sensitivity of 4.55 $mA \cdot mM^{-1} \cdot cm^{-2}$, an ultralow detection limit of 0.54 μM (S/N = 3, where N indicates response standard deviation and S represents the calibration curve's slope), and exceptional long-term stability. Significantly, this design paradigm demonstrates broad applicability, as evidenced by the successful extension to isostructural NiM-SA analogs (M = Mn, Fe, Cu) under identical synthetic conditions, establishing bimetallic 5-methylsalicylate framework as a versatile and robust electrocatalyst platform.

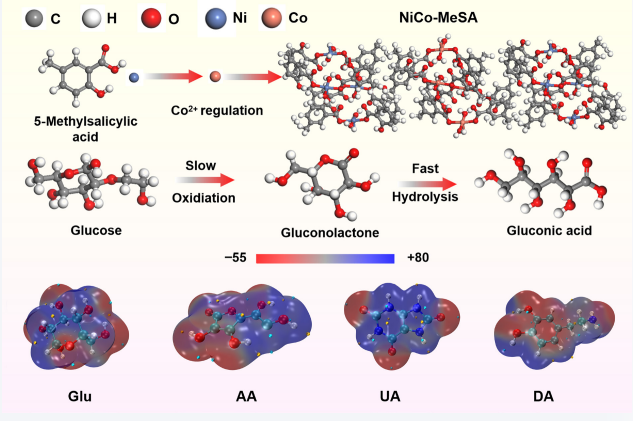

KEYWORDS: metal organic framework, glucose oxidation reaction, electrocatalyst, bimetallic 5-methylsalicylate framework

1 Introduction

Metal organic frameworks (MOFs) have emerged as a class of highly promising electrocatalytic materials for electrochemical glucose (Glu) oxidation, owing to their remarkably high specific surface area, adjustable porosity, and designable structure [1–4]. The catalytic performance of MOFs predominantly depends on the properties of their metal centers, where the metal nodes often act as active sites that promote specific chemical interactions with target analytes and thereby increasing catalytic selectivity [5–7]. However, the intrinsic limitations of single metal MOFs often hinder their performance in achieving both high sensitivity and detection stability, mainly due to restricted number of active sites and unfavorable electronic structure [8–11]. To overcome these

Received: November 4, 2025; **Revised:** December 23, 2025
Accepted: December 26, 2025

✉Address correspondence to Qing Li, 060083@yzu.edu.cn; Huan Pang, panghuan@yzu.edu.cn

limitations, introducing another type of metal ion has been demonstrated as an effective strategy to regulate the electronic structure. Enhanced electronic coupling improves both conductivity and selective adsorption, while ligand functionalization concurrently sharpens target identification [12–15], thereby achieving more efficient and sensitive glucose oxidation reactions (GORs).

Incorporating a secondary metal ion into a catalyst serves as an efficient electronic structure-tuning strategy, generating synergistic effects through electronic interactions of host and guest metals that overcome the bottleneck of sensitivity and anti-interference of single metal center catalysts at the molecular level [16–18]. Such adjustment of the electronic configuration not only stabilizes key reaction intermediates but also enhances the selectivity of electrocatalytic glucose oxidation, remarkably improving both detection sensitivity and electrocatalytic reactivity [19, 20]. Meanwhile, the presence of heterogeneous metal nodes generate abundant unsaturated coordination sites and synergistic active centers, greatly enhancing the charge transfer and yielding an enhanced current response [21–24]. More importantly, highly ordered pore structure and adjustable pore size further amplify their advantages in molecular recognition and selective adsorption [25–28]. Additionally, the formation of dual covalent bonds between organic linkers and metal sites strengthens chemical stability [29]. These collective advantages facilitate bimetallic MOFs to achieve superior performance. In the context of GOR, doping with transition metal ions (e.g., Co^{2+}, Fe^{3+}, Mn^{2+}, and Cu^{2+}) has been shown to significantly enhance the electrochemical activity of Ni-based catalysts [30–32]. Such improvement stems from synergistic electronic-interactions that promote the formation of higher-valence Ni species and stabilize key reaction intermediates along the oxidation pathway [28, 33]. Based on this rationale, Co^{2+} doping was intentionally employed in the present study to further optimize the electronic properties of the Ni based MOFs, strengthen glucose adsorption, and accelerate the kinetics of glucose to gluconate conversion [34, 35].

In this work, we report the synthesis of a series of cobalt-doped nickel 5-methylsalicate (MeSA) MOF composites (NiCo-MeSA) via a one-step solvothermal strategy. Comprehensive understanding of these materials' behavior and performance during the reaction process has been achieved by a variety angles of characterization and examination. The synergistic integration of Ni and Co not only increases the number of active sites and optimizes the electronic configuration but also reinforces the structural integrity, thereby minimizing the leaching of active components and structural collapse during catalysis. NiCo-MeSA exhibited superior sensitivity, minimal detection threshold, and excellent stability in electrochemical glucose oxidation. Furthermore, by extending this unified solvothermal synthesis route, we successfully prepared a series of NiM-MeSA MOFs (M = Mn, Fe, Cu), allowing precise regulation of redox couples through modulated metal center species. This work provides insights into the rational design of bimetallic MOF-based catalysts for high-performance electrochemical glucose oxidation.

2 Experimental

2.1 Chemicals and characterizations

All analytical-grade reagents were used as received. Nickel nitrate hexahydrate, cobalt nitrate hexahydrate, 5-methylsalicylic acid, and N,N-dimethylformamide (DMF) were purchased from Shanghai Sinopharm Chemical Reagent, while glucose and sodium hydroxide were obtained from Aladdin. Deionized water (18 MΩ·cm) was prepared at Yangzhou University. The morphologies and structures of Ni-MeSA, NiCo-MeSA-1, NiCo-MeSA-2, NiCo-MeSA-3, and Co-MeSA were characterized by scanning electron microscopy (SEM, Zeiss Supra55), transmission electron microscopy (TEM, HT7800), high-resolution TEM (HRTEM), scanning transmission electron microscopy (STEM), and elemental mapping (Tecnai G2 F30, 300 kV). Composition and crystal structure were analyzed by X-ray photoelectron spectroscopy (XPS, Thermo Scientific ESCALAB 250Xi) and X-ray diffraction (XRD, Bruker D8).

2.2 Synthesis of NiCo-MeSA

A mixture of 0.1455 g $Ni(NO_3)_3{\cdot}6H_2O$, 0.1455 g $Co(NO_3)_2{\cdot}6H_2O$, and 0.3804 g 5-methylsalicylic acid was dissolved in 60 mL DMF under thorough stirring for 15 min. Then, an aqueous solution of NaOH (0.096 g in 6 mL deionized water) was added dropwise to the mixture, followed by another 15 min of stirring. During this process, the solution turned from clear to turbid, accompanied with slight precipitation. The resulting mixture was transferred to a reaction vessel and heated at 120 °C for 3 h, during which the color deepened gradually. After cooling to room temperature, the product was collected, washed three times with DMF and ethanol, and dried at 60 °C for 24 h to obtain purple-red powder, denoted as NiCo-MeSA. NiCo-MeSA samples with varying Ni/Co ratios were synthesized following the same procedure by adjusting amounts of metal precursors (Table S1 in the Electronic Supplementary Material (ESM)).

3 Results and discussion

To gain a detailed understanding of the microstructure of a series of NiCo-MeSA samples, comprehensive characterization techniques were employed. Figure 1(a) shows the synthesis route of NiCo-MOF, and Table S1 in the ESM summarizes the detailed synthesis parameters. A series of NiCo-MOFs with different Ni/Co ratios were obtained by adjusting the molar ratios of the corresponding metal precursors. SEM depicted in Figs. 1(b1)–1(f1) and Fig. S1 in the ESM reveals the Ni-MeSA product possesses a linear and agglomerated morphology, characterized by one-dimensional (1D) nanowires that self-assembled into folded spheres structures. With the continuous incorporation of Co^{2+}, the morphology of NiCo-MeSA and Co-MeSA products remained largely unchanged, which was attributed to the similar coordination behavior of the ligand with Ni and Co. Consequently, variation in the doping ratio exerted only a minimal influence on the overall morphology of the resulting products. Figure S2 in the ESM further confirms that these self-assembled folded nanowire spheres were successfully grown on nickel foam substrates. TEM presented in Figs. 1(b2)–1(f2) and Fig. S3 in the ESM reveal that regardless of the Ni/Co doping ratios, all product exhibit linear aggregation patterns with comparable line thickness. The corresponding elemental mapping results (Figs. 1(b3)–1(f3)) show that Ni, Co, C, and O are uniformly distributed throughout the frameworks, without any obvious non-uniformity. The detailed content of each element in each sample was recorded in Table S2 in the ESM. Such uniform metal dispersion and well-maintained architecture collectively endow the NiCo-MeSA catalysts with both the electronic conductivity and

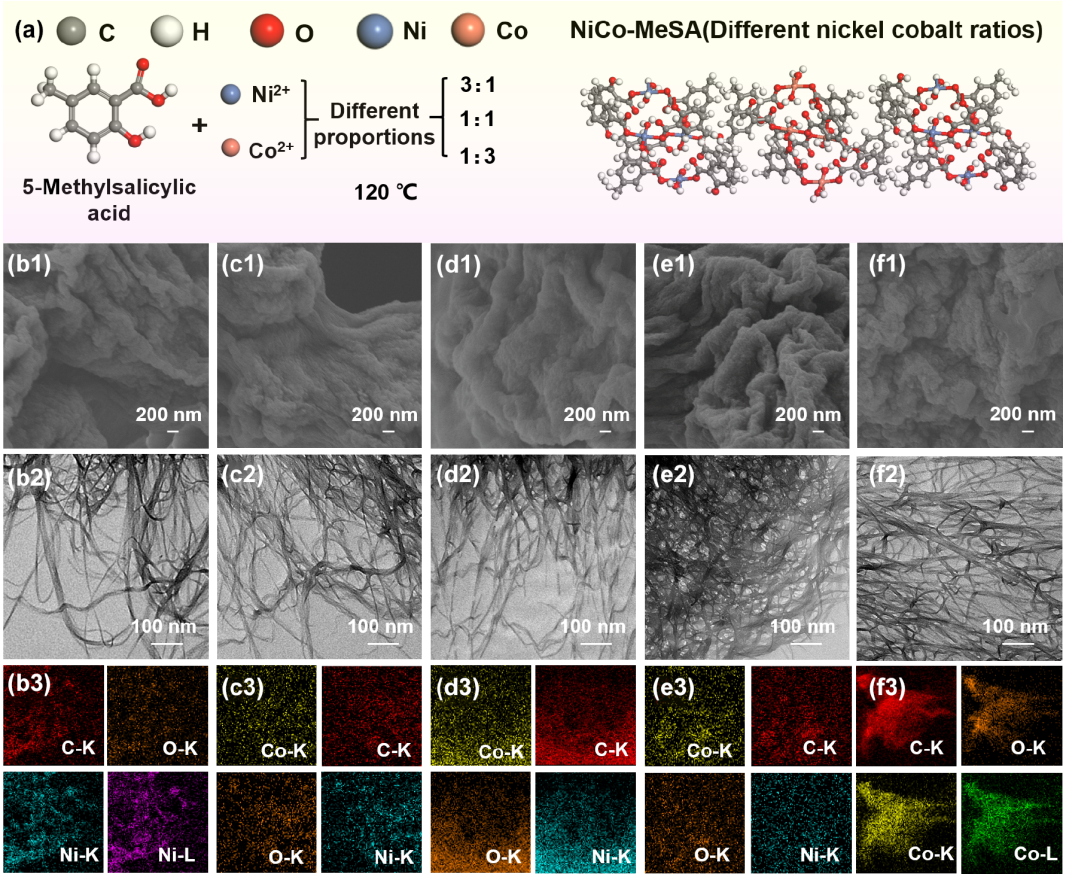

Figure 1 (a) Schematic of NiCo-MeSA sample preparation. (b1)–(f1) SEM, ((b2)–(f2)) TEM, and ((b3)–(f3)) elemental mapping for NiCo-MeSA

structural integrity, allowing it achieve superior performance in electrocatalytic GOR.

In addition, a series of bimetallic NiM-MOFs (M = Fe, Mn, Cu) with different nanostructures were synthesized via a one-step solvothermal method, as schematically illustrated in Fig. 2(a). The SEM images in Figs. 2(b1)–2(d1) and TEM images in Figs. 2(b2)–2(d2) reveal morphological variations upon metal substitution. Compared with NiCo-MOF, NiFe-MOF changed from linear aggregates to block aggregates, while NiCu-MOF exhibited amorphous shapes with a few interlaced linear substances. Notably, NiMn-MOF maintained the original self-organized folded spherical morphology of NiCo-MeSA. The elemental mapping (Figs. 2(b3)–2(d3)) confirms uniform distribution of C, O, Ni, Fe, Mn, and Cu in the low-dimensional nanomaterials. These results suggest that the different structures originate from the intrinsic coordination behavior of the specific metal.

The detailed composition and crystal structure of NiCo-MOFs with different Ni/Co ratios were analyzed using powder XRD. As shown in Fig. 3(a), the diffraction peaks of all NiCo-MOF samples closely match the simulated peak positions, indicating that the doping of Ni and Co did not induce significant lattice distortion. However, slight differences in peak intensity reflect crystal integrity caused by different doping ratios. The two faint, broad diffraction bumps, spotted at 24.8° and 42.7°, suggesting the presence of a mixed crystalline and amorphous framework. Complementarily, Fourier transform infrared spectroscopy (FTIR, Fig. 3(b) and Fig. S4 in the ESM) displays a broad peak in the range of 3200–3600 cm^{-1}, which is contributed by O–H stretching and bending vibrations [36]. The prominent peaks at 1646 and 1444 cm^{-1} arise from asymmetric (V_{as}) and symmetric (V_s) stretching vibrations of COO^-, respectively [37]. The specific surface area of NiCo-MeSA (1:1) sample was calculated to be 139.7 $m^2 \cdot g^{-1}$, as shown in Fig. 3(c). The pore size distribution of NiCo-MeSA (1:1) was studied using the Barret–Joyner–Halenda (BJH) method. The mesoporous structure with an average pore size of 4.33 nm is beneficial for catalytic sites and efficient mass transfer. The relevant data of other samples are shown in Fig. S5 and Table S3 in the ESM. The XPS (Fig. S6 in the ESM) full spectrum confirms the presence of Ni, Co, C, and O elements. The C 1s spectrum depicted in Fig. 3(d) features peaks at approximately 288.4, 286.1, and 284.5 eV, which can be attributed to covalent O=C–O, C–O, and C=C–C bonds, respectively [38]. Meanwhile, a closer look at the Ni 2p spectrum presented in Fig. 3(e) reveals two fitted peaks positioned at 873.4 and 855.8 eV, corresponding to Ni $2p_{1/2}$ and Ni $2p_{3/2}$ orbitals, characteristic of Ni^{2+} [39]. As depicted in Fig. 3(f), the Co 2p spectrum reveals two fitted peaks at 796.8 and 780.72 eV, assigned to Co $2p_{1/2}$ and Co $2p_{3/2}$, respectively [40], indicating the +2 valence state of Co in the complex. These observations verify the successful synthesis of bimetallic NiCo-MeSA with well-defined coordination environments.

In this study, the electrochemical glucose oxidation performance of NiCo-MeSA was evaluated in 0.1 M NaOH using cyclic voltammetry (CV) at scan rates ranging from 5 to 150 $mV \cdot s^{-1}$. As shown in Fig. 4(a), both anodic and cathodic peak currents increase noticeblely with scan rate, accompanied by potential shifting toward positive and negative directions, respectively. The peak current follows suit, climbing steadily in response to these changes. Moreover, as depicted in Fig. 4(b), there is a strong linear

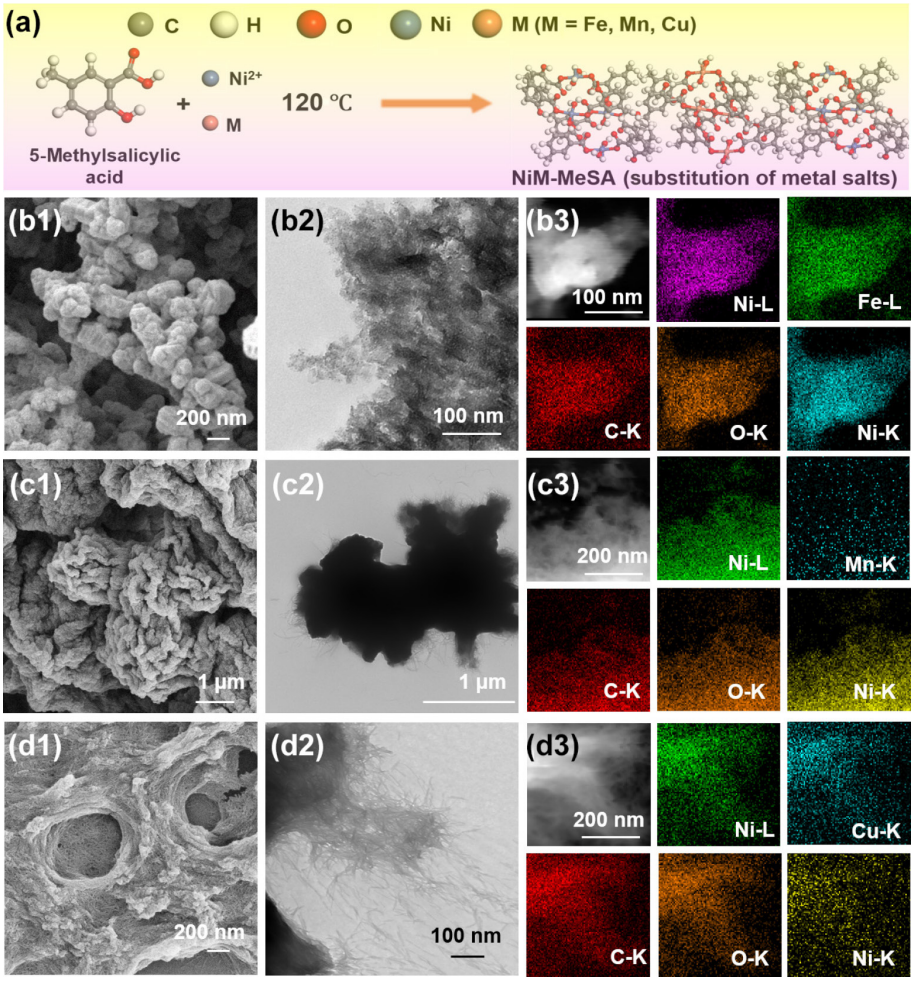

Figure 2 (a) Sample preparation schematic for metal salt substitution. (b1)–(d1) SEM, ((b2)–(d2)) TEM, and ((b3)–(d3)) elemental mapping of NiM-MeSA.

correlation between the peak current of NiCo-MeSA and the square root of the scan rate, which suggests a diffusion-controlled electrochemical process [39, 41–43]. Subsequently, CV profiles were recorded over a potential range of −0.2 to 0.8 V to evaluate the glucose oxidation performance across concentrations from 1 to 1000 μM (Fig. 4(c)). As shown, the CV response demonstrates a notable progressive increase with rising glucose concentrations, suggesting that the electrooxidation process is pivotal in the enzyme-free detection of glucose. A surge in glucose concentrations triggered a corresponding hike in electrooxidation, in turn elevating that the CV response current served as a reliable indicator of electrochemical glucose oxidation efficiency [44]. This impressive performance can be attributed to the distinctive bimetallic synergy of NiCo-MeSA, which substantially reduces the overpotential of glucose oxidation while simultaneously providing abundant active sites for the reaction. Furthermore, the inherent high specific surface area and porous structure greatly facilitate the mass transfer and reactant adsorption, thereby generating a high response current [45]. To identify the optimal applied potential, amperometric current was measured by introducing 20 μL of glucose at potentials near the peak voltage range (0.53–0.63 V). At all four voltage levels, NiCo-MeSA was capable of catalyzing the reaction of glucose. The response current exhibited consistent increase as the voltage increased from 0.53 to 0.57 V, but slightly decreased when the voltage exceeded 0.57 V. Notably, the response current at 0.6 V was the highest response value and displayed smooth performance. Consequently, 0.6 V was selected as the operating potential for all subsequent experiments (Fig. S7 in the ESM). What's more, introducing glucose solutions of varying concentrations triggered distinctive step-like current responses with the magnitude of each step increasing proportionally to glucose concentration (Fig. 4(d)). Accordingly, the data adheres to the linear correlation: I (mA) = 0.00455j + 6.01153, exhibiting a strikingly close association with an R^2 of 0.99307. This strong association between the response current and the concentration of the solution demonstrates a linear response from 55.5 to 2665.5 μM. Moreover, the calculated limit of detection (LOD) for this analysis was as low as 0.45 μM, and the sensitivity was an impressive 4.55 mA·mM^{-1}·cm^{-2}. The LOD was calculated as LOD = 3 S/N, with N indicating response standard deviation and S representing the calibration curve's slope [46]. Relative to other electrode materials (Table S4 in the ESM), NiCo-MeSA(1:1) demonstrates superior sensitivity and a lower detection limit. To verify repeatability, test was performed on NiCo-MeSA. As presented in Fig. 4(e), the pattern remained consistent throughout 10 sequential additions of 20 μL of glucose, as derived from Eq. (1)

$$\mathrm{RSD} = \frac{S}{x} \times 100\% = \frac{\sqrt{\sum_{i=1}^{n}(x_i - \bar{x})^2}}{\bar{x}} \times 100\% \quad (1)$$

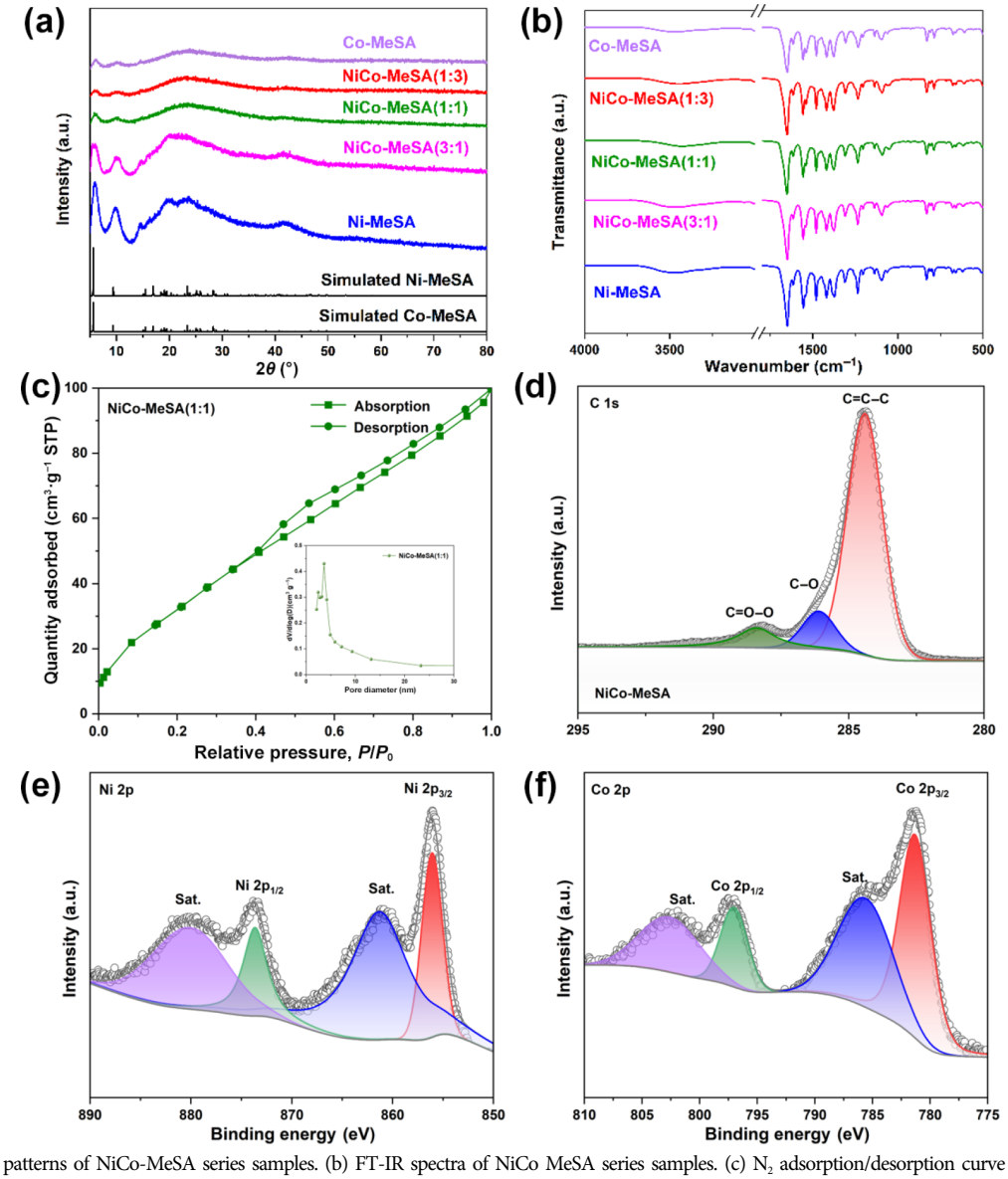

Figure 3 (a) XRD patterns of NiCo-MeSA series samples. (b) FT-IR spectra of NiCo MeSA series samples. (c) N_2 adsorption/desorption curve of NiCo-MeSA (1:1) (embedded figure shows pore size distribution). XPS spectra of (d) C 1s, (e) Ni 2p, (f) Co 2p.

The response currents' relative standard deviation (RSD) was determined as 3.22%, signifying high consistency in NiCo-MeSA's response to glucose [47] (S: standard deviation; $\bar{x}$: mean the average of multiple measurements; x_i: the results of each test; n: actual measurement frequency). The electrochemical data for the rest of the NiCo-MeSA series samples can be seen in Figs. S8–S11 in the ESM. The anti-interference capability of NiCo-MeSA was evaluated by sequentially introducing glucose and various common interfering substances. As depicted in the stable current (i)–time (t) curve in Fig. S12 in the ESM, the interferents caused no noticeable dips in the response current, confirming the strong selectivity and anti-interference ability of NiCo-MeSA. Moreover, even faced with multiple interferents, the NiCo-MeSA consistently delivered a robust electrical signal to glucose without any diminishment in its intensity, underscoring its immense commercial viability. Long-term stability was further assessed (Fig. S13 in the ESM), where the current response remained consistent for the entire 8-h duration continuous test, signifying its exceptional electrochemical stability and its suitability for prolonged testing. As shown in the Fig. 4(f), a comprehensive comparison of various electrochemical indicators of all NiCo-MeSA samples reveals that NiCo-MeSA (1:1) exhibited the best electrochemical glucose oxidation performance, indicating that an optimized Ni/Co ratio significantly enhances catalytic activity through synergistic effects between the two metal centers. This conclusion is confirmed by a comprehensive performance comparison within other catalysts (Table S5 in the ESM).

In order to delve deeper into the origin of the remarkable selectivity of NiCo-MeSA toward certain prevalent small biomolecules, first-principles calculations were conducted to examine its electrophilic characteristics. In general, molecules sporting a more positive ESP (it refers to the electrostatic interaction energy felt by a unit positive charge at a certain position in the space around a molecule or atom) tend to have a greater knack for drawing in nucleophilic species (or electron donors), making them more favorable for selective molecular recognition. The three-dimensional (3D) ESP mapping illustrated in Fig. 5(a) provides valuable insights into the electronic features of these four biological molecules. A closer look reveals that the Glu molecule

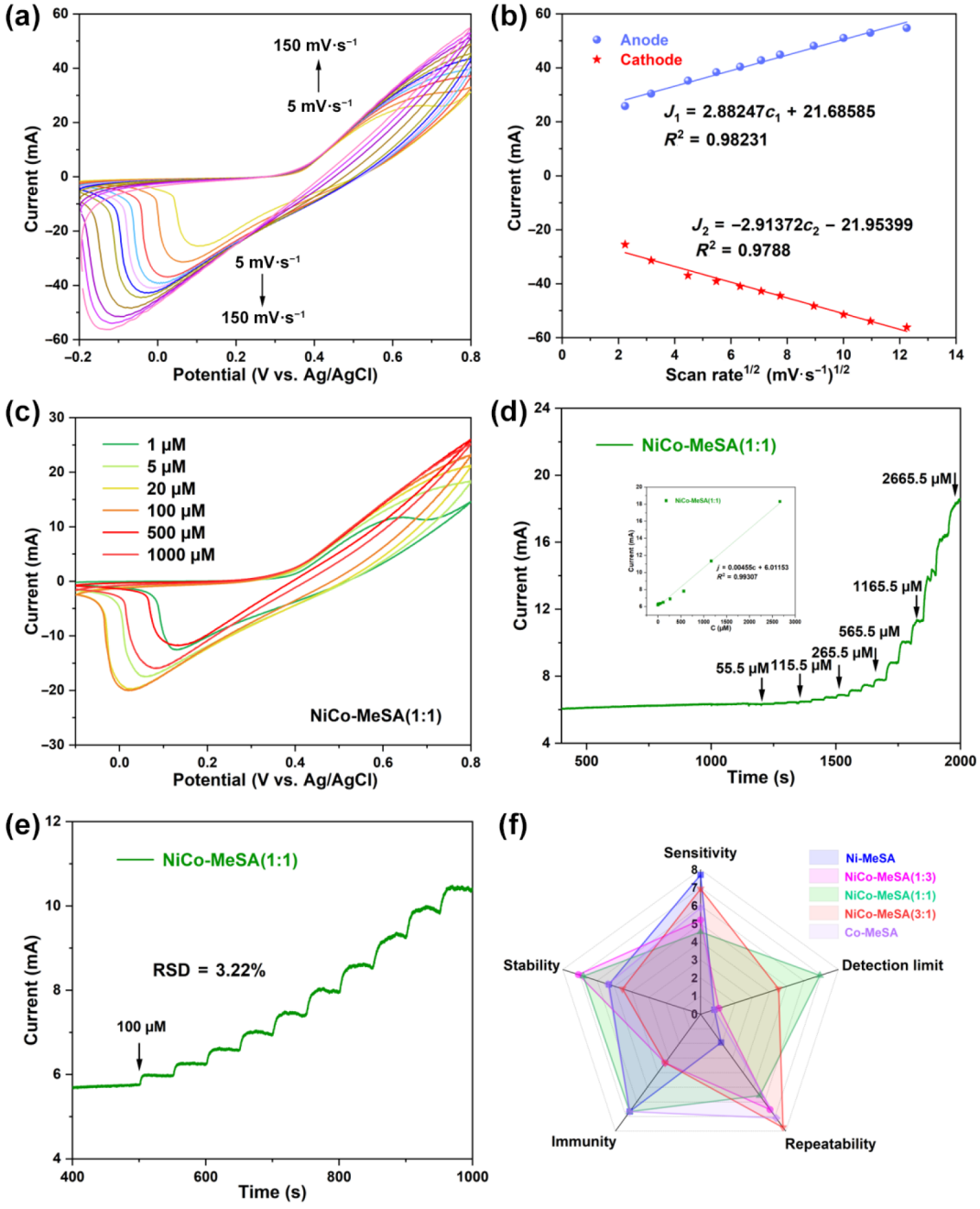

Figure 4 (a) CV analysis of NiCo-MeSA (1:1) across varying scan rates. (b) Evaluation of peak current density versus scan rate square root for NiCo-MeSA (1:1). (c) NiCo-MeSA CV variability across glucose concentrations (50 mV·s^{-1} scan rate). (d) Amperometric signal from NiCo-MeSA (1:1) upon incremental glucose introduction (inset: linear calibration validation for NiCo-MeSA (1:1) with sequential glucose dosing). (e) Reproducibility trend of NiCo-MeSA (1:1). (f) Radar plot of all samples' electrochemical properties.

sports several local positive ESP peaks (+64.42, +38.67, +27.69, +18.65, and +13.06 kcal·mol^{-1}) scattered throughout its molecular space, and has along with only two negative local minima separated and located at opposite ends of the molecule. In contrast, uria (UA), ascorbic acid (AA), and dopamine (DA) molecules also exhibit considerable local positive ESP maxima but with a more dispersed distribution and multiple strong negative local minima (e.g., −49.07, −44.62, and −42.06 kcal·mol^{-1}) in their vicinity. This significantly weakens their ability to attract electron donors. Overall, the glucose molecule demonstrates the most extensive and positive ESP distribution among the four biological molecules, indicating its superior ability to interact with nucleophilic reagents [48, 49]. Experimental evidence indicates the reaction pathway shown in Fig. 5(b). At the outset, glucose molecules diffuse through the alkaline electrolyte and work their way into the porous NiCo-MeSA framework, where they latch onto the active sites. Once adsorbed, chemical interactions are established between glucose and the NiCo-MeSA surface. Subsequently, the hemiacetal C–H bonds in glucose undergo cleavage, forming fresh chemical bonds on the electrode surface. Concurrently, under the combined influence of the alkaline medium and applied potential, NiCo-MeSA is gradually oxidized to NiOOH and CoOOH, thereby promoting the conversion of

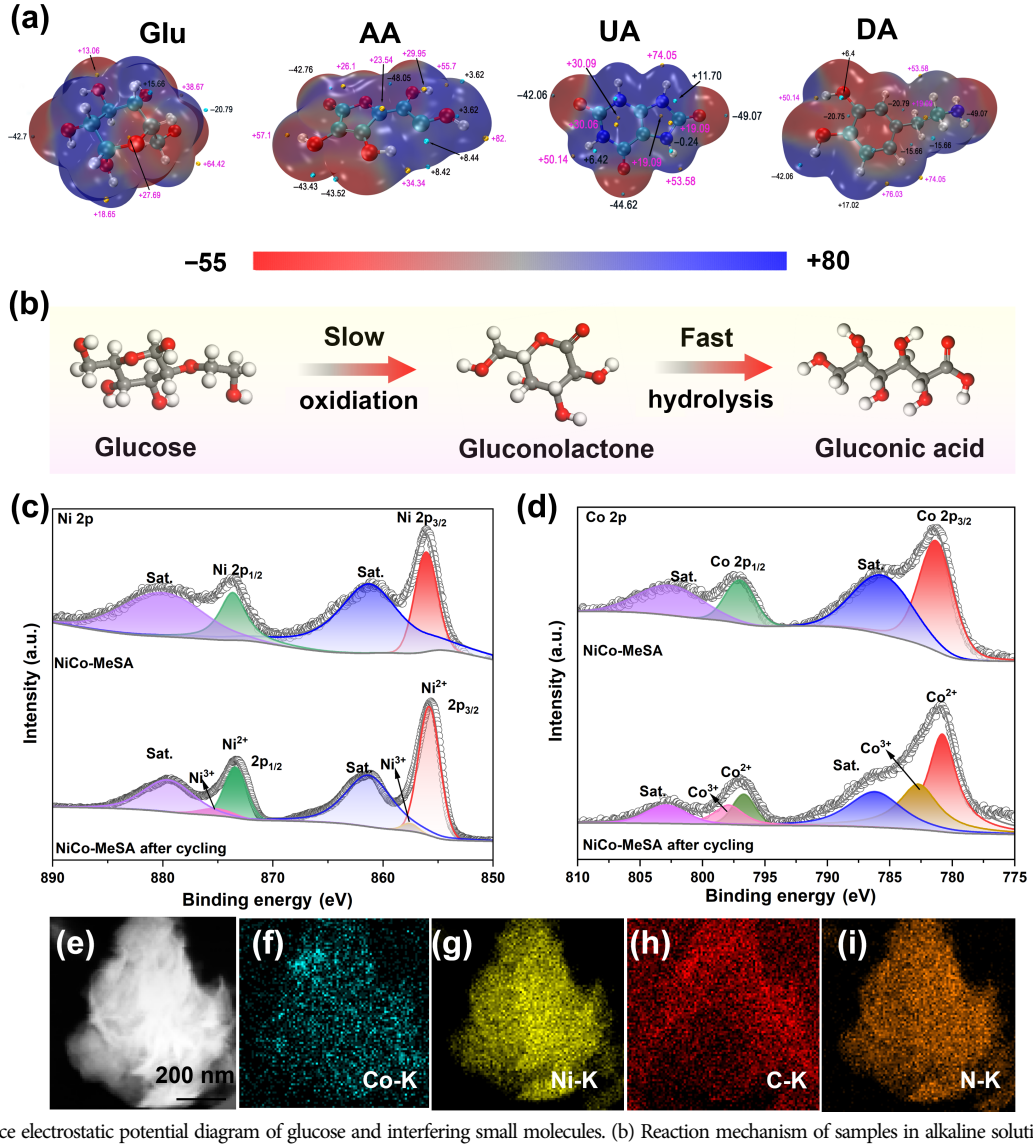

Figure 5 (a) Surface electrostatic potential diagram of glucose and interfering small molecules. (b) Reaction mechanism of samples in alkaline solution. Comparison of XPS spectra before and after reaction: (c) Ni 2p and (d) Co 2p. (e)–(i) STEM images and elemental mapping of NiCo-MeSA after testing.

glucose to gluconic acid. Further XPS analysis (Figs. 5(c) and 5(d)) provides the valence change during the electrochemical process. The Ni $2p_{3/2}$ peaks at 855.67 eV (Ni^{2+}) and 857.56 eV (Ni^{3+}) after cycling evidenced the Ni^{2+} peak in the post-cycled sample have undergone a subtle shift of approximately 0.2 eV toward lower binding energy when compared to the pristine material. This slight but discernible change suggests a minor electronic redistribution following electrochemical cycling process. Also, a similar change is observed for the Co species. Elemental analysis (Figs. 5(e)–5(i)) demonstrated that Ni, Co, C, and O were uniformly distributed on the surface of the post-reacting NiCo-MeSA. The increased oxygen level results from the generation of $Ni(OH)_2$, $Co(OH)_2$, NiOOH, and CoOOH compounds.

4 Conclusions

In summary, a series of NiCo-MeSA composite materials with varying NiCo doping ratios were successfully synthesized via one-step solvothermal method by adjusting the input amounts of metal nickel cobalt salts. The study revealed that when the NiCo ratio was optimized to 1:1, the material performed excellently in the GOR system. With the help of the synergistic effect of the two metal ions, NiCo-MeSA achieved a high sensitivity of 4.55 $mA{\cdot}mM^{-1}{\cdot}cm^{-2}$, a detection limit as low as 0.54 μM, and superior reaction stability. The efficient GOR originates from the bimetallic synergistic effect, which optimizes the electronic structure, reduces the reaction energy barrier, improves the electrocatalytic efficiency, and effectively suppresses metal leaching and skeleton collapse, ensuring long-term stability. This study provides valuable insights into the design and application of bimetallic MOF catalysts for enzyme-free GOR.

Electronic Supplementary Material: Supplementary material is available in the online version of this article at https://doi.org/10.26599/NR.2026.94908377

Data availability

All data needed to support the conclusions in the paper are presented in the manuscript and the Electronic Supplementary

Material. Additional data related to this paper may be requested from the corresponding author upon request.

Acknowledgements

This work was supported by the Natural Science Research Project of Guangling College, Yangzhou University (No. ZKZD25003), the National Natural Science Foundation of China (No. 52371240), the Key Basic Research Program of Jiangsu Province (No. BK20253046), Yangzhou Innovation Capability Enhancement Fund/program (No. SCX2025020017), the Universities' Philosophy and Social Science Researches in Jiangsu Province (No. 2023SJYB2088), and Jiangsu Donghua Analytical Instrument Co., Ltd. (No. DH7000D), and the technical support we received at the Testing Center of Yangzhou University.

Declaration of competing interest

All the contributing authors report no conflict of interests in this work. Author Huan Pang is the editorial board member of this journal, but he is not involved in the peer-review or decision of this article.

Author contribution statemen

Q. L. conceived the idea and designed and engineered the samples; Y. L., D. H. W., B. Y. T., and S. Z. C. performed the experiments; Y. L., B. H., M. S., and X. Y. Q. wrote the paper with support from Q. L.; P. H. supervised the project. All authors contributed to the general discussion.

Use of AI statement

None.

References

[1] Chen, P.; Wang, T. Y.; He, D.; Shi, T.; Chen, M. F.; Fang, K.; Lin, H. Z.; Wang, J.; Wang, C. Y.; Pang, H. Delocalized isoelectronic heterostructured $FeCoO_xS_y$ catalysts with tunable electron density for accelerated sulfur redox kinetics in Li-S batteries. *Angew. Chem., Int. Ed.* **2023**, *62*, e202311693.

[2] Gouda, A.; Hannouche, K.; Mohan, A.; Mao, C. L.; Nikbin, E.; Carrière, A.; Ye, J.; Howe, J. Y.; Sain, M.; Hmadeh, M. et al. *In-situ* restructuring of Ni-based metal organic frameworks for photocatalytic CO_2 hydrogenation. *Nat. Commun.* **2025**, *16*, 695.

[3] Sun, Y.; Liu, P. F.; Xie, Y.; Tian, Z.; Wang, X.; Zheng, W. H.; Jiang, Z. Y.; Kang, Z.; Zhang, Y. Programmable active phase reconstruction in metal-organic framework toward high-efficient oxygen evolution. *Adv. Mater.* **2025**, *37*, e09664.

[4] Li, S. L.; Zhou, Z. X.; Li, J. H.; Xiao, Y.; Yuan, Y.; Zhu, H.; Cui, F. C.; Jing, X. F.; Zhu, G. S. Reversible surface reconstruction of metal-organic frameworks for durable oxygen evolution reaction. *Chem. Sci.* **2025**, *16*, 12568–12576.

[5] Qiu, Z. M.; Guo, X. T.; Cao, S.; Du, M.; Wang, Q. C.; Pi, Y. C.; Pang, H. High-entropy Ag-Ru-based electrocatalysts with dual-active-center for highly stable ultra-low-temperature zinc-air batteries. *Angew. Chem., Int. Ed.* **2025**, *64*, e202415216.

[6] Su, Y. C.; Zhang, Y. F.; Feng, W. C.; Zhang, G. X.; Sun, Y. Y.; Yin, C. H.; Yuan, G. Q.; Tang, Y. J.; Zhou, W. F.; Chen, H. C. et al. Monocarboxylic acid structural analogues facilitate *in situ* composite of functional complexes for aqueous batteries. *Angew. Chem., Int. Ed.* **2025**, *64*, e202502752.

[7] Guo, X. T.; Xu, H. Y.; Qiu, Z. M.; Li, Q.; Li, N. N.; Yang, Z. B.; Li, W. T.; Lian, Y.; Li, Q.; Sui, Y. W. et al. Heteroatom-modulated asymmetric cobalt single-atom catalysts on MOF-derived carbon enabling durable zinc-iodine batteries. *Adv. Mater.* **2025**, *37*, e14035.

[8] Baby, N.; Thangarasu, S.; Murugan, N.; Kim, Y. A.; Lee, J. M.; Oh, T. H. Versatile bimetallic metal-organic framework with nanocutting channels tailored for efficient electrocatalytic water oxidation and glucose detection. *J. Alloys Compd.* **2024**, *970*, 172601.

[9] Yue, K. H.; Lu, R. H.; Gao, M. B.; Song, F.; Dai, Y.; Xia, C. F.; Mei, B. B.; Dong, H. L.; Qi, R. J.; Zhang, D. L. et al. Polyoxometalated metal-organic framework superstructure for stable water oxidation. *Science* **2025**, *388*, 430–436.

[10] Zheng, S. S.; Sun, Y.; Xue, H. G.; Braunstein, P.; Huang, W.; Pang, H. Dual-ligand and hard-soft-acid-base strategies to optimize metal-organic framework nanocrystals for stable electrochemical cycling performance. *Natl. Sci. Rev.* **2022**, *9*, nwab197.

[11] Chowdhury, S.; Nugraha, A. S.; O'May, R.; Wang, X. H.; Cheng, P.; Xin, R. J.; Osman, S. M.; Hossain, M. S.; Yamauchi, Y.; Masud, M. K. et al. Bimetallic metal-organic framework-derived porous one-dimensional carbon materials for electrochemical sensing of dopamine. *Chem. Eng. J.* **2024**, *492*, 152124.

[12] Wang, H.; Yang, L.; Yang, Y. N.; Jia, L. S. Multifunctional bimetallic MOF engineering: Innovative synthesis and versatile applications in adsorption, catalysis, sensing, and energy. *Coord. Chem. Rev.* **2026**, *547*, 217114.

[13] Arunkumar, P.; Gayathri, S.; Rajasekar, A.; Senthil Kumar, S.; Kumar Kamaraj, S.; Hun Han, J. Lewis acidic Fe^{3+}-driven catalytic active Ni^{3+} formation in Fe-free metal-organic framework for enhanced electrochemical glucose sensing. *J. Colloid Interface Sci.* **2024**, *656*, 424–439.

[14] Li, J. H.; Jiang, Y.; Zhang, X.; Huo, Y. D.; Du, F. L.; Tuo, Y. X.; Guo, Z. Y.; Chen, D. W.; Chen, S. H. Efficiently coupled glucose oxidation for high-value D-glucaric acid with ultradurable hydrogen via Mn(III) in acidic solution. *Nano Res.* **2023**, *16*, 10748–10755.

[15] Zhang, L. J.; Zhang, T. T.; Zhao, Y. L.; Dong, G. F.; Lv, S. K.; Ma, S. L.; Song, S. X.; Quintana, M. Doping engineering of lithium-aluminum layered double hydroxides for high-efficiency lithium extraction from salt lake brines. *Nano Res.* **2024**, *17*, 1646–1654.

[16] Zhang, J.; Zhuang, X. L.; Meng, W.; Tong, B. R.; Liu, L.; Wang, Y.; Han, C. Dual-confinement regulating ternary metal-oxide activity sites derived from Co-MOF for enhanced electrocatalytic activity for glucose oxidation. *Chem. Eng. J.* **2024**, *489*, 151398.

[17] Guo, Y. T.; Rinawati, M.; Chang, L. Y.; Li, C.; Ho, C. J.; Shi, P. C.; Chen, K. J.; Huang, W. H.; Mizuguchi, H.; Yeh, M. H. Fine-tuning the Ni/Co ratio to elucidate the coordination structure-activity relationship of MOF-derived bimetallic layered double hydroxides for highly sensitive enzyme-free lactate biosensors. *Nanoscale* **2025**, *17*, 20207–20218.

[18] Zhang, Y.; Huang, Q. L.; Sun, Z. H.; Zheng, R.; Ma, Y. M.; Han, D. X.; Niu, L. A wearable electrochemical sensor based on single-atom Pt anchored on activated NiCo-LDH/$Ti_3C_2T_x$ for real-time monitoring of glucose. *Anal. Chem.* **2024**, *96*, 18239–18245.

[19] Shi, W. J.; Lu, T. B. Recent advances in MOF-based dual-atom catalysts for CO_2 reduction. *Chem. —Eur. J.* **2025**, *31*, e202500636.

[20] Liu, S.; Qiu, Y. Z.; Liu, Y. F.; Zhang, W. F.; Dai, Z.; Srivastava, D.; Kumar, A.; Pan, Y.; Liu, J. Q. Recent advances in bimetallic metal-organic frameworks (BMOFs): Synthesis, applications and challenges. *New J. Chem.* **2022**, *46*, 13818–13837.

[21] Wei, L. Z.; Hossain, M. D.; Chen, G.; Kamat, G. A.; Kreider, M. E.; Chen, J. J.; Yan, K.; Bao, Z. N.; Bajdich, M.; Stevens, M. B. et al. Tuning two-dimensional phthalocyanine dual site metal-organic framework catalysts for the oxygen reduction reaction. *J. Am. Chem. Soc.* **2024**, *146*, 13377–13390.

[22] Yuan, H. M.; Weng, C. Y.; Zhang, X. H.; Chen, L. G.; Zhang, Q.; Ma, L. L.; Liu, J. G. Construction of bifunctional MOF-based composite electrocatalysts promoting oxygen evolution reaction and glucose

oxidation reaction and its kinetic deciphering. *Mater. Today Phys.* **2024**, *49*, 101601.

[23] Wang, Z. G.; Hu, Y.; Yang, W. L.; Zhou, M. J.; Hu, X. Facile one-step microwave-assisted route towards Ni nanospheres/reduced graphene oxide hybrids for non-enzymatic glucose sensing. *Sensors* **2012**, *12*, 4860–4869.

[24] Liu, W. J.; Liu, W. X.; Hou, T.; Ding, J. Y.; Wang, Z. G.; Yin, R. L.; San, X. Y.; Feng, L. G.; Luo, J.; Liu, X. J. Coupling Co–Ni phosphides for energy-saving alkaline seawater splitting. *Nano Res.* **2024**, *17*, 4797–4806.

[25] Chen, K. L.; Chou, Y. H.; Lin, T. J.; Cheng, M. J.; Hsiao, P. K.; Pu, Y. C.; Chen, I. W. P. Real-time monitoring of Fe-induced stable γ-NiOOH in binder-free FeNi MOF electrocatalysts for enhanced oxygen evolution. *Small* **2025**, *21*, 2501142.

[26] Zheng, F. B.; Lin, T.; Wang, K.; Wang, Y. L.; Li, G. D. Recent advances in bimetallic metal-organic frameworks and their derivatives for thermal catalysis. *Nano Res.* **2023**, *16*, 12919–12935.

[27] Xu, D.; Cao, X. L.; Zhou, J.; Lin, Z. H.; Wang, J.; Han, J. T.; Chen, G.; Liu, G. Y.; Xu, X. M.; Zhang, Y. G. et al. Analysis of microstructure properties of Ni-Fe MOFs and their influence on selective recognition of single and binary dye systems. *npj Clean Water* **2025**, *8*, 35.

[28] Zhao, J. J.; Wang, Y. J.; Wu, Y. P.; Xia, W.; Chang, X. W.; Wu, X. Q.; Li, S.; Li, D. S. Chiral Ni-MOFs as bifunctional electrochemical platform for efficient alcohol oxidation and highly sensitive non-enzymatic glucose detection. *Nano Res.* **2025**, *18*, 94907930.

[29] Zhang, Y.; Xu, Y.; Li, N.; Ma, W. H.; Yang, M.; Hou, C. J.; Huo, D. Q. An ultra-sensitive dual-signal ratio electrochemical aptasensor based on functionalized bimetallic MOF nanocomplexes by the *in-situ* electrochemical synthesis for detect HER2. *Int. J. Hydrogen Energy* **2023**, *48*, 24548–24558.

[30] Wei, Y. H.; Hui, Y. X.; Lu, X. J.; Liu, C. Z.; Zhang, Y. L.; Fan, Y. J.; Chen, W. One-pot preparation of NiMn layered double hydroxide-MOF material for highly sensitive electrochemical sensing of glucose. *J. Electroanal. Chem.* **2023**, *933*, 117276.

[31] Yu, K.; Li, X. W.; Zhan, S. Q.; Chai, H. N.; Cao, X. Y.; Cao, F. F.; Guan, J.; Xu, Q. G.; Gao, X. Z.; Qu, L. J. et al. Programmable bimetallic MOF nanozyme composite with microenvironment-adaptive cascade catalysis for wearable glucose biosensing and accelerated diabetic wound healing. *Anal. Chem.* **2025**, *97*, 21668–21678.

[32] Zhu, R. M.; Song, Y. Z.; Hu, J. L.; Zhu, K. D.; Liu, L. M.; Jiang, Y. X.; Xie, L. R.; Pang, H. Conductive metal-organic framework grown on the nickel-based hydroxide to realize high-performance electrochemical glucose sensing. *Chem. —Eur. J.* **2024**, *30*, e202400982.

[33] Wang, G. W.; Hu, K.; Liu, J. Q.; Zhang, Z. Q.; Li, Z. J.; Qu, Y.; Yu, B.; Li, Z.; Wang, Y. G.; Li, H. Y. et al. *Nicotiana tabacum* growth promotion by water oxidation modulated artificial photosynthesis with Ru-Oxo clusters decorated g-C_3N_4 nanosheets. *Nano Res.* **2025**, *18*, 94907498.

[34] Zha, X. T.; Yang, W. Y.; Shi, L. W.; Li, Y.; Zeng, Q.; Xu, J. H.; Yang, Y. J. Morphology control strategy of bimetallic MOF nanosheets for upgrading the sensitivity of noninvasive glucose detection. *ACS Appl. Mater. Interfaces* **2022**, *14*, 37843–37852.

[35] Li, P. P.; Bai, Y.; Zhang, G. X.; Guo, X. T.; Meng, X. R.; Pang, H. Surface-halogen-introduced 2D NiCo bimetallic MOFs via a modulation method for elevated electrochemical glucose sensing. *Inorg. Chem. Front.* **2022**, *9*, 5853–5861.

[36] Devic, T.; Horcajada, P.; Serre, C.; Salles, F.; Maurin, G.; Moulin, B.; Heurtaux, D.; Clet, G.; Vimont, A.; Grenéche, J. M. et al. Functionalization in flexible porous solids: Effects on the pore opening and the host-guest interactions. *J. Am. Chem. Soc.* **2010**, *132*, 1127–1136.

[37] Peng, J.; Zhang, W.; Wang, J. S.; Li, L.; Lai, W. H.; Yang, Q. R.; Zhang, B. W.; Li, X. N.; Du, Y. M.; Liu, H. W. et al. Processing rusty metals into versatile prussian blue for sustainable energy storage. *Adv. Energy Mater.* **2021**, *11*, 2102356.

[38] Su, Y. C.; Hu, J. L.; Yuan, G. Q.; Zhang, G. X.; Wei, W. X.; Sun, Y. Y.; Zhang, X. X.; Liu, Z.; Suen, T. N.; Chen, H. C. et al. Regulating intramolecular electron transfer of nickel-based coordinations through ligand engineering for aqueous batteries. *Adv. Mater.* **2023**, *35*, 2307003.

[39] Guo, X. T.; Zhao, J. W.; Wang, J.; Li, B.; Meng, X. R.; Zhai, W. W.; Pang, H. Uniform nickel nanoparticles decorated porous carbon nanofibers for efficient electrochemical nitrite sensing. *Mater. Today Chem.* **2024**, *41*, 102344.

[40] Yang, B.; Shi, Y. X.; Song, G. J.; Pei, C. G.; Yan, Y.; Chen, Z. D.; Pang, H. Bimetallic design based on the nucleation rate of prussian blue analogues for enhanced aqueous zinc ion batteries with glycerol-water hybrid electrolytes. *Angew. Chem., Int. Ed.* **2025**, *137*, e202425391.

[41] Wang, F.; Hu, J. L.; Wu, X. H.; Yuan, G. Q.; Su, Y. C.; Fan, Z. H.; Xue, H. G.; Pang, H. Streamlined synthesis of superstructure Ni-benzimidazole MOFs: Glucose electrochemical analysis. *J. Colloid Interface Sci.* **2024**, *665*, 764–771.

[42] Wang, F.; Hu, J.; Liu, Y.; Yuan, G.; Zhang, S.; Xu, L.; Xue, H.; Pang, H. Turning coordination environment of 2D nickel-based metal-organic frameworks by π-conjugated molecule for enhancing glucose electrochemical sensor performance. *Mater. Today Chem.* **2022**, *24*, 100885.

[43] Li, Q.; Zhang, G. X.; Xu, Y. X.; Sun, Y. Y.; Pang, H. P-regulated hierarchical structure Ni_2P assemblies toward efficient electrochemical urea oxidation. *Acta Phys. - Chim. Sin.* **2024**, *40*, 2308045.

[44] Zhou, Y. X.; Zhang, L.; Li, J. L.; Hu, M. Y.; Zhuang, G. Q.; Xiong, X. L. Novel self-supporting CoNi-MOF with triangular cone geometry array structure for highly sensitive electrochemical sensing of fructose in beverages. *Colloids Surf. A Physicochem. Eng. Asp.* **2025**, *719*, 137045.

[45] Zhong, Y. J.; Zhang, N.; Lyu, Q. L.; Waqas, M.; Liu, C. Z.; Lu, L. J.; Xu, S. Y.; Fan, Y. J.; Liu, G.; Chen, W. Oxygen vacancy-engineered porous nicu MOF@LDHs for highly sensitive electrochemical glucose sensing. *Electroanalysis* **2025**, *37*, e70036.

[46] Huang, W.; Yang, Y.; Xu, Y.; Xiao, F.; Wang, L. Sweat wearable sensor based on confined Pt nanoparticles in 2D conductive metal-organic frameworks for continuous glucose monitoring. *Adv. Sci.* **2025**, *12*, e07212.

[47] Dong, S.; Yuan, X.; Chen, Y. Y.; Liu, B. L.; Dai, R. X.; Dai, F. Y.; Xiang, M.; Yang, Z. Assembling of self-supported metal-organic framework aerogel heterojunction for enhancing glucose sensing. *J. Environ. Chem. Eng.* **2025**, *13*, 116041.

[48] Zou, J.; Wu, S. L.; Liu, Y.; Sun, Y. J.; Cao, Y.; Hsu, J. P.; Shen Wee, A. T.; Jiang, J. Z. An ultra-sensitive electrochemical sensor based on 2D g-C_3N_4/CuO nanocomposites for dopamine detection. *Carbon* **2018**, *130*, 652–663.

[49] Meng, W.; Wen, Y. Y.; Dai, L.; He, Z. X.; Wang, L. A novel electrochemical sensor for glucose detection based on Ag@ZIF-67 nanocomposite. *Sensors Actuat. B: Chem.* **2018**, *260*, 852–860.